Improved Physical Optics Computation Near the Forward Scattering Region: Application to 2-D Scenarios

Thomas Pairon, Christophe Craeye, *Senior Member, IEEE*, and Claude Oestges, *Fellow, IEEE*

***Abstract*— The classical physical optics (PO) formulation of the scattered fields suffers from the loss of accuracy when the observation angle widely deviates from the specular direction. This is even worse in the "forward region," i.e., for the bistatic angles between 90° and 270°. The method presented in this article aims at improving the accuracy of the fields in this region by finding the currents induced on the nonilluminated part of the object, where the classical PO assumes zero currents. The proposed approach reformulates the initial problem using equivalent currents over a domain surrounding the object. The equivalent currents then act as new sources that induce electrical currents computed by the classical PO formulation. The computation of the equivalent problem is accelerated using the multipole expansion of Green's function, including appropriate singularity extraction in the very near field. This approach provides an error that is significantly lower in the forward direction than the classical PO formulation. The principles of this new approach are presented and validated for the 2-D scenarios.**

***Index Terms*— Bistatic radar cross section (RCS), equivalence theorem, fast multipole method (FMM), forward scattering, magnetic-field integral equation (MFIE), physical optics (PO), shadowing.**

I. Introduction

FORWARD scattering plays a significant role in many wireless applications. For example, it strongly impacts the power transmitted or received by an antenna located in the vicinity of a large structure (such as cars or planes) [1]; it may also be viewed as nearly canceling the incident field during blockage, for instance, shadowing by humans in the millimeter-wave indoor communications [2]. Forward-scattering radars are another relevant example, which exploit the enhanced radar cross section (RCS) of a target when the angle between the transmitter and the receiver is close to 180° [3]. In these conditions, the RCS is often computed using Babinet's principle [4], where the scattered fields in the forward direction (i.e., for a bistatic angle equal to 180°) correspond to the fields radiated by an aperture having the same silhouette as the considered target; however, this method does no longer hold when the bistatic angle significantly deviates from 180°.

Therefore, RCS predictions are usually obtained using different numerical methods offering various levels of complexity and accuracy. Among them, the method of moments (MoM) provides a very high accuracy, with an error level driven by the mesh size, at the expense of high memory and computational complexities [respectively, $\mathcal{O}(N^2)$ and $\mathcal{O}(N^3)$ for the direct solvers, with N the number of discretizing functions]. To overcome those limitations, one may employ the asymptotic methods, approximating acceptably the scattered fields when the electrical size of the target is very large. Among the asymptotic methods, the physical optics (PO) approximation [5] produces a moderate error level. This method describes quite precisely a variety of scattering mechanisms, while offering a complexity that grows linearly with the electrical surface of the object.

While PO provides a satisfactory estimation of the fields at an observation point near the specular direction, as well as for a bistatic angle $\phi = 180°$, the accuracy on the fields deteriorates significantly in the forward region [6]–[8], defined by the bistatic angles $\phi \in [90°, 270°]$. The reason is that PO delivers a good approximation of the equivalent currents on the illuminated part of the surface but lacks accuracy near the shadow boundary and in the nonilluminated region of the scatterer where it assumes zero currents. A better estimation of the currents in those regions is, thus, required for a more accurate evaluation of the fields in the forward region.

In the literature, the PO currents on the shadowed parts of the objects are obtained using the iterative PO (IPO) method, initially developed for the resonances in the open cavities [9]. In a nutshell, the initial PO currents (computed by the classical formulation) act as new sources inducing in turn the currents on the parts of the object visible from these new currents. This has been extended to the general scenarios involving resonances, such as concave objects [10], [11]: ships [12], tanks [13], or antennas mounted on large platforms [1]. The IPO is also used when different objects interact with each other, so that an object in the forward region of another one induces currents on the shadow part after reflection on the surface of the former [14], [15]. In other words, the currents on the shadowed surfaces computed with IPO correspond to those induced by a reflection on the surrounding objects (if any) but do not model the currents due to the diffraction by the scatterer itself. In particular, IPO cannot compute currents in

Manuscript received August 21, 2019; revised April 24, 2020; accepted June 20, 2020. Date of publication July 16, 2020; date of current version January 5, 2021. This work was supported by the Fonds pour la formation à la Recherche dans l'Industrie et l'Agriculture (FRIA) Grant of the Belgian Fonds National de la Recherche Scientifique (FNRS) Fund. *(Corresponding author: Thomas Pairon.)*

The authors are with the Institute of Information and Communication Technologies, Electronics and Applied Mathematics (ICTEAM), Université catholique de Louvain, 1348 Louvain-la-Neuve, Belgium (e-mail: thomas.pairon@uclouvain.be).

Color versions of one or more of the figures in this article are available online at https://ieeexplore.ieee.org.

Digital Object Identifier 10.1109/TAP.2020.3008669

the nonilluminated part of the object when the studied scenario involves a single scatterer.

Unlike the abovementioned works, the method proposed here does not require reflections on any other nearby entities to estimate the currents on the unlit part of an isolated scatterer. To the best of our knowledge, such capabilities are not yet available in the literature. Starting from the total fields obtained with the classical PO, electric and magnetic currents are computed on a surface enclosing the scatterer by invoking the equivalence theorem [16, Sec. 3.5]. By superposition, those currents in turn radiate magnetic fields that induce new currents computed with the classical PO on the whole object. We emphasize that the proposed method, as an improved version of the classical PO, does not truly compete with the MoM in terms of accuracy.

As for the classical PO formulation, the proposed method is a current-based approach: once the equivalent currents representing the scattering problem have been computed, the fields scattered in any direction of observation are computed easily. This can, for instance, be done very efficiently using the method described in [17]. This is not the case for other asymptotic approaches, such as the uniform theory of diffraction (UTD). Using this ray-based method, the diffracted field at a particular observation point in the shadow region depends on the incident field where the ray hits the surface and on the point from which the ray leaves the surface toward the observation point, thus requiring a new computation for every pair of source and observation points [18], [19].

This article is structured as follows. Section II illustrates the limitations of the classical PO formulation based solely on the electrical currents for the perfect electric conductors (PECs). As presented in Section III, the proposed method overcomes those limitations using the electric and magnetic equivalent currents, accelerated with the fast multipole method (FMM). The results for PEC bodies in two dimensions are given in Section IV, where the scattered fields are compared for the MoM reference solution, the classical PO method, and the proposed approach. The conclusions and perspectives end this article in Section V.

II. Limitations of the Classical PO

PO is a current-based asymptotic method with an $\mathcal{O}(N)$ complexity, where N is the number of discretizing functions representing an object surface. It is, therefore, very suitable for the prediction of scattering by electrically large structures, where the full-wave methods fail due to their computational complexity. The PO method replaces the physical object by equivalent currents $\mathbf{J}_{\mathrm{PO}}$ radiating in free space. Assuming a PEC, those currents are expressed as

$$\mathbf{J}_{\mathrm{PO}} = \begin{cases} 2\,\hat{\mathbf{n}} \times \mathbf{H}_{\mathrm{i}} & \text{on the “lit” region} \\ 0, & \text{on the “unlit” region} \end{cases} \quad (1)$$

with $\hat{\mathbf{n}}$ the outward normal of the surface and $\mathbf{H}_{\mathrm{i}}$ the incident magnetic field on the object surface. The “lit” region encompasses the part of the surface that is in line of sight with the source, while the “unlit” region is the complementary part.

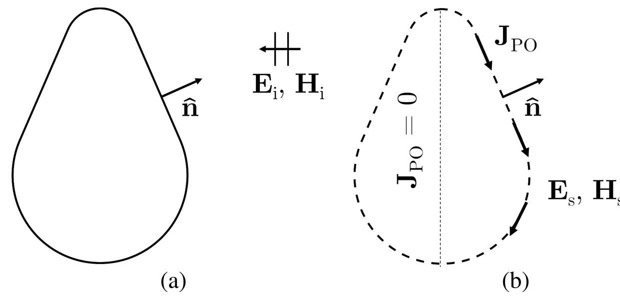

Fig. 1. (a) Initial scattering problem. (b) Equivalent problem with PO currents on the illuminated part of the object.

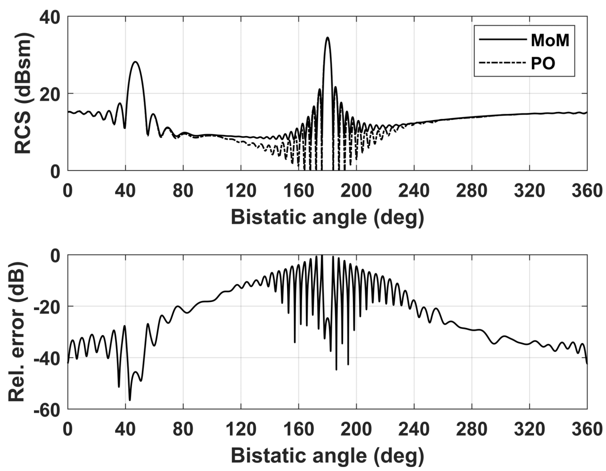

Fig. 2. Bistatic RCS of the problem depicted in Fig. 1, computed with MoM (reference) and the classical PO. Bottom: relative error of the scattered fields.

In the case of a convex object, those regions are defined for a point $\mathbf{r}$ belonging to the surface S as

$$\mathbf{r} \in S : \begin{cases} \hat{\mathbf{k}}_i \cdot \hat{\mathbf{n}}(\mathbf{r}) \leqslant 0, & \text{defines the “lit” region} \\ \hat{\mathbf{k}}_i \cdot \hat{\mathbf{n}}(\mathbf{r}) > 0, & \text{defines the “unlit” region} \end{cases}$$

where $\hat{\mathbf{k}}_i$ is the wave vector of the incident field. For the concave objects, or when many objects are involved, different techniques allow the determination of the “lit” region, such as geometrical visibility [20], [21] or shadow radiation [11], [14], [15].

To illustrate the validity and limitations of (1), consider the problem depicted in Fig. 1. The initial problem consists of a PEC smooth scatterer [Fig. 1(a)] complying with the abovementioned criteria and an incident wave (taken here as a plane wave, although this is not mandatory) propagating from right to left. The equivalent PO problem is presented in Fig. 1(b), where the PO currents are computed on the lit region according to (1).

The bistatic RCS of the considered object is shown in Fig. 2, where the PO solution is compared with a full-wave MoM reference. The bottom graph depicts the relative error on the scattered fields, defined as

$$\text{Rel. error} = 10\log_{10}\frac{|f_{\mathrm{MoM}} - f_{\mathrm{PO}}|^2}{|f_{\mathrm{MoM}}|^2}\ (\mathrm{dB}) \quad (2)$$

where f_{MoM} and f_{PO} stand for the scattered field amplitude obtained with the help of the MoM and the PO solutions, respectively. One can observe that in the vicinity of the specular region (around 45°), the PO solution is in good agreement with the exact result. The approximation is also valid in the vicinity of the forward direction (observation angle close to 180°). Besides those two aforementioned regions, the PO approximation in its classical formulation does not hold, providing an inaccurate estimation of the fields when the observation angle ϕ lies in the forward region, roughly defined as $\phi \in [90°,\ 270°]$. Similar effects have been observed in previous works [6], [22], [23].

These discrepancies arise because the PO does not accurately represent the currents near the shadow boundary [23] and assumes as null the currents on the backside of the scatterer. Different approaches have been proposed for the modeling of those currents on the convex objects. Fock's theory [24] proposes an asymptotic representation of the currents near the boundary between the lit and the shadowed region, within a region of length $d = (\lambda\rho^2/\pi)^{1/3}$, where ρ is the radius of curvature at the boundary [24]. Although providing a very accurate solution for simple geometries, this approach does not enable a uniform description of the currents for the arbitrary convex shapes [25]. An improvement in the PO formulation is proposed in [26], where a new normal vector is defined, which depends on the incident and observation angles, and thus requires a new computation for every observation point.

In this work, our goal is to provide a good approximation of the currents in the shadow boundary, as well as in the deep shadowed part of the surface, in order to improve the accuracy of the fields computed behind the scatterer. The method derives the surface currents flowing on the surface of the scatterer. The solution depends only on the incident field, as opposed to other techniques that require the *a priori* knowledge of the scattering direction.

III. New Formulation of the PO

A. Update of the Currents via an Equivalent Problem

Let us consider a PEC convex body bounded by a surface S and with sources $(\mathbf{J}_{\mathrm{i}}, \mathbf{M}_{\mathrm{i}})$ located outside S and radiating the incident fields, as depicted in Fig. 3(a). As a first guess, the total PO fields $\mathbf{E}_{\mathrm{t}}$ and $\mathbf{H}_{\mathrm{t}}$ are obtained by the classical PO approximation and are the sum of the incident fields $(\mathbf{E}_{\mathrm{i}}, \mathbf{H}_{\mathrm{i}})$ and the fields radiated by the PO currents [see Fig. 3(a)]. It is possible to derive an internal equivalent problem [16, Sec. 3.5], so that the total PO fields inside the equivalence surface S' are exactly described by the new equivalent electric and magnetic currents $\mathbf{J}_{\mathrm{e}}$ and $\mathbf{M}_{\mathrm{e}}$ (respectively) flowing on S'. Outside S', the fields are set as null [see Fig. 3(b)], so that the equivalent currents are computed as

$$\mathbf{J}_{\mathrm{e}} = \hat{\mathbf{n}}' \times (0 - \mathbf{H}_{\mathrm{t}}) \tag{3}$$
$$-\mathbf{M}_{\mathrm{e}} = \hat{\mathbf{n}}' \times (0 - \mathbf{E}_{\mathrm{t}}). \tag{4}$$

The electric and magnetic fields $\mathbf{E}_{\mathrm{e}}, \mathbf{H}_{\mathrm{e}}$ radiated by the equivalent currents defined above are computed as follows [27, Sec. 3.4]:

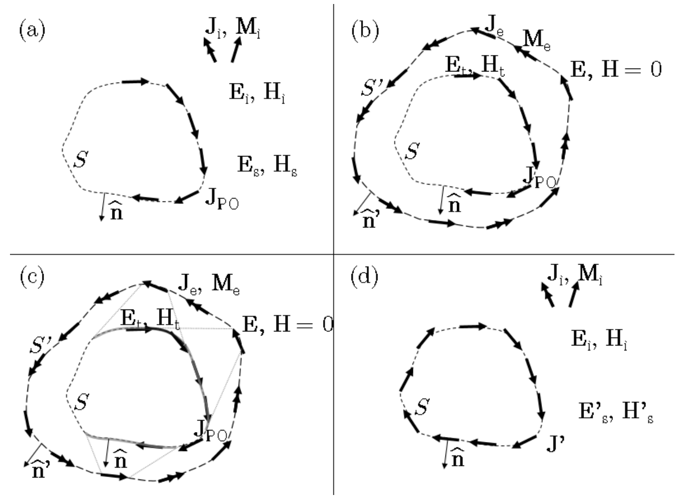

Fig. 3. Different steps for updating the PO currents. Magnetic currents (double arrows) exist only on the equivalence surface S', while the original surface S only supports the electric currents (simple arrow). (a) Initial problem. (b) Equivalent problem. (c) Re-radiation on the surface. (d) Updated currents.

$$\mathbf{E}_{\mathrm{e}} = -j\omega\mu\left(\mathbf{A} + \frac{1}{k^2}\nabla\nabla\cdot\mathbf{A}\right) - \nabla\times\mathbf{F} \tag{5}$$
$$\mathbf{H}_{\mathrm{e}} = \nabla\times\mathbf{A} - j\omega\epsilon\left(\mathbf{F} + \frac{1}{k^2}\nabla\nabla\cdot\mathbf{F}\right) \tag{6}$$

where $\mathbf{A}$ and $\mathbf{F}$ are, respectively, defined by

$$\mathbf{A} = \int_{S'} \mathbf{J}_{\mathrm{e}} G(\mathbf{r}, \mathbf{r}')\mathrm{d}S' \tag{7}$$
$$\mathbf{F} = \int_{S'} \mathbf{M}_{\mathrm{e}} G(\mathbf{r}, \mathbf{r}')\mathrm{d}S'. \tag{8}$$

In (5) and (6), μ is the vacuum permeability, ϵ is the vacuum permittivity, j is the imaginary unit, $\omega = 2\pi f$, where f is the frequency, $k = 2\pi/\lambda$ is the wavenumber, $\mathbf{r}$ is the observation point coordinate, $\mathbf{r}'$ is the source coordinate and belongs to S', and $G(\mathbf{r}, \mathbf{r}') = -(j/4)H_0^{(2)}(k|\mathbf{r} - \mathbf{r}'|)$ is 2-D Green's function. The differential operators apply on the observation coordinates. Full derivation for a TM incident wave is provided in Appendix A.

The current distribution can be represented as a weighted sum of basis functions $\mathbf{f}^i$ with weights $\mathbf{j}_{\mathrm{e}}^i$ and $\mathbf{m}_{\mathrm{e}}^i$, so that (3) and (4) are now read as

$$\mathbf{J}_{\mathrm{e}} = \sum_i \mathbf{j}_{\mathrm{e}}^i \mathbf{f}^i \tag{9}$$
$$\mathbf{M}_{\mathrm{e}} = \sum_i \mathbf{m}_{\mathrm{e}}^i \mathbf{f}^i. \tag{10}$$

Among different types of basis functions, the pulse basis functions are used in this article and are defined as

$$\mathbf{f}_i(l) = \begin{cases} 1, & l^i \le l \le l^{i+1} \\ 0, & \text{elsewhere} \end{cases} \tag{11}$$

where l corresponds to a coordinate along the object boundary.

The new electric currents $\mathbf{J}'$ on the object are then computed as follows: each elementary electric and magnetic current

$\mathbf{J}_{\mathrm{e}}^{i}$ and $\mathbf{M}_{\mathrm{e}}^{i}$ associated with basis function i on S' radiate a magnetic field through (6) on $S^{\mathrm{vis}(i)}$, defined as the portion of S that is visible from the source basis function i. This process is illustrated in Fig. 3(c), where one can observe that $S^{\mathrm{vis}(i)} \bigcap S^{\mathrm{vis}(i+1)} \neq \varnothing$. The modified electric currents $\mathbf{J}'$ on $S^{\mathrm{vis}(i)}$ are then computed as

$$\mathbf{J}'^{\mathrm{vis}(i)} = 2\,\hat{\mathbf{n}} \times \mathbf{H}_{\mathrm{e}}^{\mathrm{vis}(i)} \tag{12}$$

where $\mathbf{H}_{\mathrm{e}}$ stands for the magnetic field (6) re-radiated by the equivalent currents. The contributions from each portion of S' are added up, thus providing modified electric currents on the whole surface of the object [Fig. 3(d)]. Redistributing the incident source on an equivalence surface enclosing the scatterer allows one to illuminate the latter from every angle, thereby also illuminating the shadowed zone.

In [15], electric and magnetic currents are also used for the PO calculations. The modified PO electric and magnetic currents extend over the whole structure, regardless of the visible or shadowed regions, producing nearly zero fields in the deep shadow behind the scatterer. This approach bypasses any visibility testing procedure for the isolated objects or the multiple scattering scenarios. This is different from our approach, for which the electric and magnetic currents are located on an equivalence surface surrounding the object and illuminate the shadowed part of it.

B. Acceleration Through Multipole Expansion

Obtaining the equivalent currents requires the computation of the total fields from the initial PO problem [see (5) and (6)]. This operation is the bottleneck of the proposed method; if it is performed naively, the computational complexity is $\mathcal{O}(MN)$, with (M, N) the number of basis functions on S and S', respectively. The number of operations is large, since the standard PO approximation is valid for the objects conforming to $kR \gg 1$. This difficulty is addressed with the help of the FFM [28]. This method and its multilevel implementation [multilevel fast multipole algorithm (MLFMA)] [29] are usually employed in an MoM context for reducing the computation time and the memory requirement by speeding up the matrix-vector products, enabling the analysis of scattering by large structures [30]–[32].

In this article, the FMM speeds up the computation of (5) and (6). This starts from writing Green's function between a basis function located at a point $\mathbf{r}_n$ near $\mathbf{r}_{n'}$ and a testing function located at a point $\mathbf{r}_m$ near $\mathbf{r}_{m'}$ in the 2-D case as [33]

$$G(\mathbf{r}_m, \mathbf{r}_n) = \frac{1}{2\pi}\int_C P'(\mathbf{r}_{n'}, \hat{\alpha}) \cdot T(\mathbf{r}_{n'm'}, \hat{\alpha}) \cdot P(\mathbf{r}_{m'}, \hat{\alpha})\,\mathrm{d}C \tag{13}$$

$$P'(\mathbf{r}_{n'}, \hat{\alpha}) = \exp(jk\hat{\alpha} \cdot \mathbf{r}_{nn'}) \tag{14}$$

$$P(\mathbf{r}_{m'}, \hat{\alpha}) = \exp(-jk\hat{\alpha} \cdot \mathbf{r}_{mm'}) \tag{15}$$

where C is the unit circle, $\hat{\alpha}$ is a vector pointing on C from its center, and $T(\mathbf{r}_{m'n'}, \alpha)$ is the translation operator defined in Appendix B. Other variables in (13) are defined in Fig. 4.

Equation (13) suggests that all the interactions between two groups of basis functions whose centers are far from each other (typically more than one wavelength) are expressed as a product between the radiation patterns of the transmitting (14) and receiving (15) groups, and a translation operator that depends on the relative positions between the centers of the groups. Once the radiation patterns of the transmitting and receiving groups have been computed, one can rapidly obtain all MN interactions between the N basis functions of the transmitting group centered at $\mathbf{r}_{n'}$ and the M testing functions of the receiving group centered at $\mathbf{r}_{m'}$. Doing so, the computational complexity reduces from $\mathcal{O}(N^2)$ to $\mathcal{O}(N^{3/2})$. For more details on the FMM, the reader is referred to [27], [28], [33], and [34]. The partial derivatives of Green's functions involved in the computation of the fields in (5) and (6) can also be decomposed with the FMM, and we derive them in Appendix C.

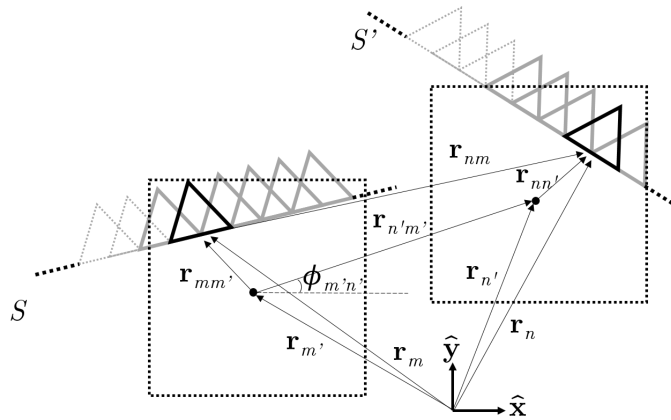

Fig. 4. Geometry of the multipole expansion of 2-D Green's function. Gray triangles represent the discretizing functions and black triangles represent the chosen basis and testing functions. The dashed boxes represent the border of the FMM groups, with centers' positions $\mathbf{r}_{m'}$ and $\mathbf{r}_{n'}$.

The multipole expansion is valid for the transmitting and receiving groups that are "far" from each other (Appendix B), typically for $\mathbf{r}_{nm} > \lambda$. For close interactions, Green's function is integrated explicitly as in (5) and (6). Note that when S and S' are close to each other, the numerical integration of Green's function requires a high number of sampling points due to the singularity of Green's function and its partial derivatives at the origin. The computational complexity of this numerical integration is reduced with an analytical singularity extraction, as suggested in [35]–[39]. The singular part of the integrand is subtracted, thus strongly reducing the number of points required for the numerical integration of the nonsingular part. This result is added to the analytical integral of the singular part, which is written as

$$\iint I\,\mathrm{d}\mathbf{r}'\mathrm{d}\mathbf{r} = \underbrace{\iint (I - I_s)\,\mathrm{d}\mathbf{r}'\mathrm{d}\mathbf{r}}_{\text{non-singular: numerical}} + \underbrace{\iint I_s\,\mathrm{d}\mathbf{r}'\mathrm{d}\mathbf{r}}_{\text{singular: analytical}} \tag{16}$$

where I is the integrand found in (5) and (6) invoking Green's function or one of its partial derivatives, and the subscript s stands for the singular part of I. Singularity extraction for Green's function can be found in the abovementioned articles, and an example for the derivative of 3-D Green's function is available in [38]. The singular parts of the derivatives of

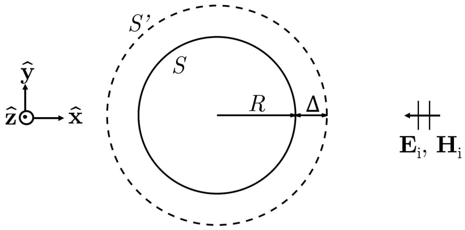

Fig. 5. Cylinder with a circular section under plane-wave incidence. The PEC surface is represented by the solid line, while the equivalence surface is represented by the dotted line.

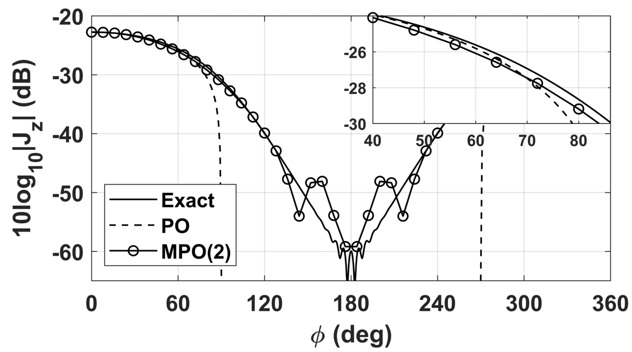

Fig. 6. Magnitude of the currents obtained from three different methods for a TM polarization. MPO(2) stands for the solution obtained with the proposed method after two iterations. Inset: zoomed-in view around the shadow boundary.

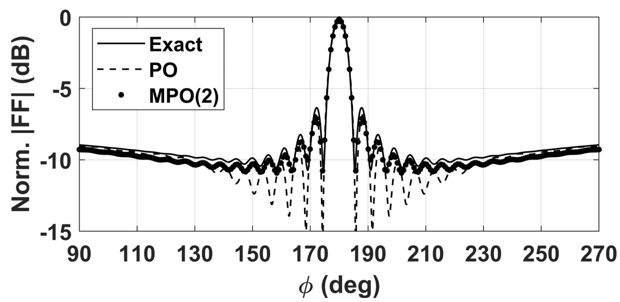

Fig. 7. Normalized far-field radiation pattern of the cylinder under TM incidence in the forward region $\phi \in [90^\circ, 270^\circ]$.

2-D Green's functions are provided in Appendix D. A similar derivation is found in [40].

IV. Numerical Results

This section presents the results obtained by the exact solution (analytical or by a full-wave MoM simulation), the classical PO approximation, and the proposed method for various test cases. The given examples consist of infinitely long cylinders with different convex contours, except for an attempt for a concave contour. The examples are, thus, considered as the 2-D problems. Nevertheless, the proposed method can be generalized to the 3-D problems, as it relies on the PO, equivalence principle, and FMM, all valid in 3-D. The excitation comes from a plane wave, although the method is not restricted to this type of excitation. Except for the cylinder with a circular cross section (Section IV-A2), the incident electric field is aligned with the cylinder axis (TM case). Surfaces are discretized with the pulse basis functions of maximal length $\lambda/8$ for the PO and the proposed method. For the MoM solution, the surface is sampled at $\lambda/15$. Except for the cylinder with a circular section that admits an analytical solution, other reference solutions are computed with the MoM code.

A. Circular section

1) TM Polarization: As a first example, we consider the cylinder with a circular section of radius $R = 5\lambda$ represented in Fig. 5, with the electric field polarization parallel to the cylinder axis $+\hat{z}$ (TM case) propagating toward $-\hat{x}$. The equivalence surface S' is also represented and has the same shape as the cylinder, with a radius $R' = R + \Delta$, with $\Delta = \lambda/10$. The impact on this parameter will be discussed later (Section IV-A3). This canonical problem admits an analytical solution for the surface currents, given by [16, Sec. 5.9]

$$\mathbf{J}_z = \frac{-2}{\omega\mu\pi R}\sum_{n=-\infty}^{\infty}\frac{j^{-n}e^{jn\phi}}{H_n^{(2)}(kR)}. \tag{17}$$

The comparison among the exact series solution (17), the standard PO formulation, and the proposed approach (named MPO in the following figures) is displayed in Fig. 6. It is observed that the MPO solution provides a good approximation of the currents near the shadow boundary [24] (the boundary between the lit and unlit regions), where the PO solution starts to deteriorate. Note that for the parts of the scatterer located in the deep lit region, the PO provides a slightly better approximation of the MoM currents (inset of Fig. 6), although the simulation results show that this does not have a significant impact on the accuracy of the scattered fields.

The normalized far-field radiation pattern is illustrated in Fig. 7. In the exact backscattering direction ($\phi = 0^\circ$), the PO (as well as MPO) matches with the exact solution [22]. The fictitious zeros appearing with the PO solution around the forward region [periodically located at $\phi = \pi \pm n(\lambda/(2R))$] are reduced by the proposed method.

2) TE Polarization: Let us now consider the same problem of Fig. 5 with the electric field aligned with $-\hat{y}$ and still propagating toward $-\hat{x}$ (TE case), with the same dimension parameters. The analytical solution for the surface currents is given as [16, Sec. 5.9]

$$\mathbf{J}_\phi = \frac{2j}{\omega\mu\pi R}\sum_{n=-\infty}^{\infty}\frac{j^{-n}e^{jn\phi}}{H_n^{(2)'}(kR)}. \tag{18}$$

From Fig. 8, one can observe that the modified PO approach smoothens the abrupt current transition between the lit and unlit regions, as obtained by the classical PO, which assumes the magnitude of the currents is constant on the illuminated region. The comparison between the radiation patterns is presented in Fig. 9, where the contribution of the proposed method is quite obvious in the forward region.

3) Impact of the Parameter Δ: The proposed method relies on a single parameter Δ that corresponds to the distance between the object and the surface on which the intermediate equivalent currents are computed. The authors observed that the smaller the Δ, the better the approximation of the currents.

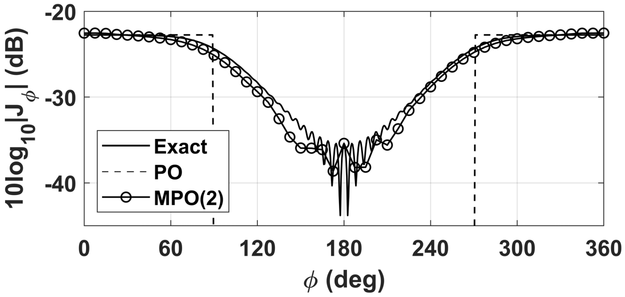

Fig. 8. Magnitude of the currents for the TE polarization.

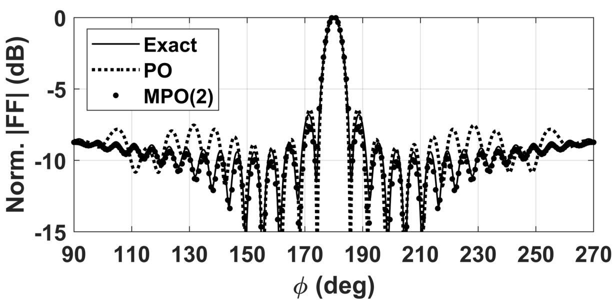

Fig. 9. Normalized far-field radiation pattern of the cylinder under TE incidence in the forward region ($\phi \in [90^\circ, 270^\circ]$).

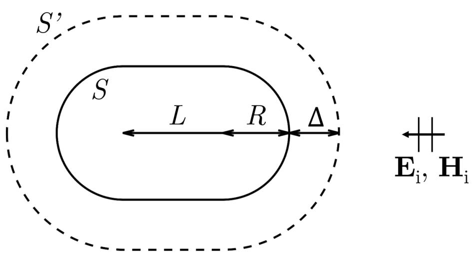

Fig. 10. Cylinder with an elongated section under plane-wave incidence (TM case).

Nevertheless, one should ensure that, on the one hand, at least one basis function of S is visible by each discretizing function on S'. That implies that if S and S' are too close to each other, the spatial sampling of the surface should be increased, thus increasing the computation time and the memory required for the computation of the near-field interactions. On the other hand, when a pair of basis functions on S and S' are very close, despite singularity extraction, a larger number of integration points is required for the computation of the equivalent currents due to the singular behavior of Green's function for small $\mathbf{k}|\mathbf{r}-\mathbf{r}'|$ (see Section III-B). As a rule of thumb, choosing the distance parameter as $\Delta \approx$ size l of the basis functions is a good tradeoff between the accuracy and the computational complexity.

B. Elongated Cylinder

The second example is illustrated in Fig. 10. The section of this cylinder corresponds to two half disks of radius $R = 5\lambda$ connected by a rectangle of length $L = 10\lambda$ and width $2R$. This is an example of interest, since the initial PO currents are the same as that in the problem analyzed in Section IV-A1.

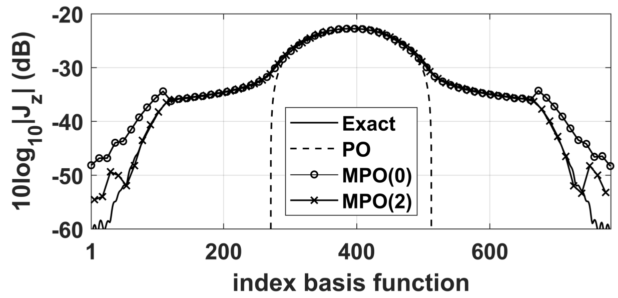

Fig. 11. Current distributions for the problem of Fig. 10 (TM case).

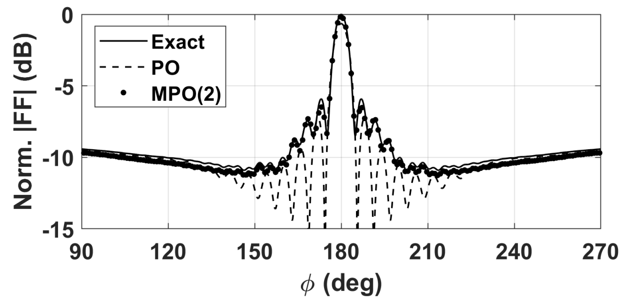

Fig. 12. Normalized far-field radiation pattern of the elongated cylinder ($R = 5\lambda and L = 10\lambda$) under TM incidence in the forward region ($\phi \in [90^\circ, 270^\circ]$).

Indeed, the PO currents are assumed null if $\hat{\mathbf{n}} \cdot \hat{\mathbf{k}}_i = 0$ (i.e., the surface is parallel to the incident propagation vector). The surface currents are displayed in Fig. 11. The modified PO solution approximates quite accurately the currents on the flat part of the object, within a 0.1 dB absolute error, whereas the classical PO assumes null currents on that part. The results for the MPO at iterations 0 and 2 are compared. One can observe that for iteration 0, the proposed approach induces an abrupt change in the current distribution, located at the transition between the flat surface and the shadowed part. Those current spurts are damped after an additional iteration; thus, the MPO provides a good approximation of the exact solution, even for small current intensities. The number of additional iterations is fixed to 2 (hence, a total of three iterations, including the initial evaluation), which does not impact significantly the computation time, as discussed in Section IV-D. Since the method is based on the tangent-plane approximation (the same applies for the classical PO), it is not expected that more iterations yield convergence toward the exact solution.

The radiation pattern corresponding to this problem in the forward region is provided in Fig. 12. The fields radiated by the PO solution are the same as those presented in Fig. 7, since the PO current distribution is the same for both examples. One can conclude that the proposed approach efficiently deals with the curvature discontinuities [41] and the nose-on illuminations for the strongly elongated bodies, where the standard PO fails [42]. The radiation pattern of a magnified version of the problem ($R = 50\lambda$, $L = 100\lambda$) is also provided in Fig. 13. This shows that the proposed PO approach also contributes to a better estimation of the scattered fields for larger problems.

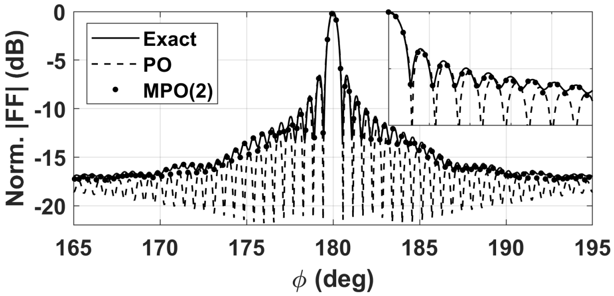

Fig. 13. Normalized far-field radiation pattern of the elongated cylinder ($R = 50\lambda and L = 100\lambda$) under TM incidence in the forward region. For a better visibility, the azimuth observation angle is limited to $\phi \in [165^\circ, 195^\circ]$. Inset: zoomed-in view of the radiation pattern for $\phi \in [180^\circ, 185^\circ]$.

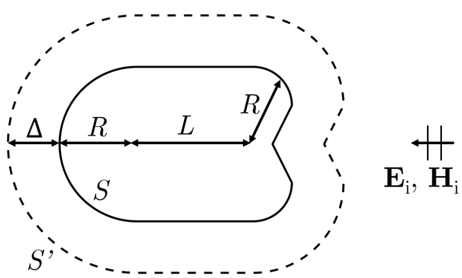

Fig. 14. Cylinder with an elongated section and a concave part under the plane-wave incidence (TM case).

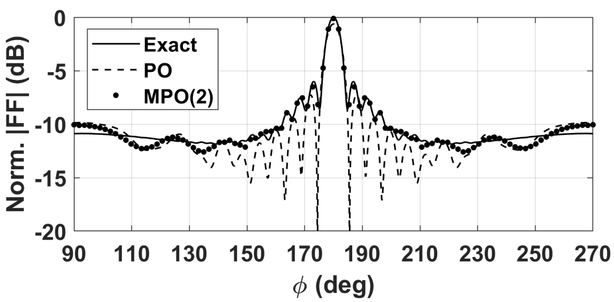

Fig. 15. Normalized far-field radiation pattern of the elongated cylinder with a concave part ($R = 5\lambda and L = 10\lambda$) under TM incidence in the forward region ($\phi \in [90^\circ, 270^\circ]$).

Due to its large dimensions, the reference solution of this problem has been computed by an MoM-FMM approach.

A variation in this problem is illustrated in Fig. 14, where a concave corner has been added to the half-circle facing the incident-wave direction. The angle of the corner is chosen large enough in order to reduce the effect of the higher order reflections. The geometries inducing multiple scatterings may be analyzed using the proposed approach combined with IPO, but are outside the scope of this article. The comparison of the radiation pattern for this example is provided in Fig. 15, with a noticeable improvement on the accuracy of the scattered fields in the forward region, despite the little concave part in the contour, while the classical PO performs better in the backward region.

C. Fields Behind a Scatterer

The following example analyzes the field distribution in the vicinity of the scatterer in the forward region. The previous examples focused on the far-field radiation pattern, while the proposed improvement in PO also provides a better estimation of the fields in the close vicinity of the scatterer. This region is of particular interest in different applications, such as electromagnetic compatibility, stealth technology, antennas installed on vehicles [1], and weather radar blockage by wind turbines [43]. The proposed modification of the PO method greatly improves the accuracy of the fields in the region behind the object. Let us consider the same example as before, with the scatterer in Fig. 10. The total electric field computed with MoM is illustrated in Fig. 16, where the dashed lines represent different cuts in which the total field obtained with PO and the proposed approach are compared in Fig. 17. The proposed method performs better than PO in the vicinity of the surface, as shown in Fig. 17(a) and (b). The poor performance of PO is expected due to the specific geometry of the problem, since the approximation does not hold for the grazing incidence. The farther the observation, the better the accuracy of both PO and the proposed method. However, the method described here significantly outperforms the classical PO for any presented scenario, with an absolute error below -30 dB for any observation in the forward region. The error is higher right behind the scatterer, where the object obstructs substantially the incident wave, producing a total field with a very small amplitude.

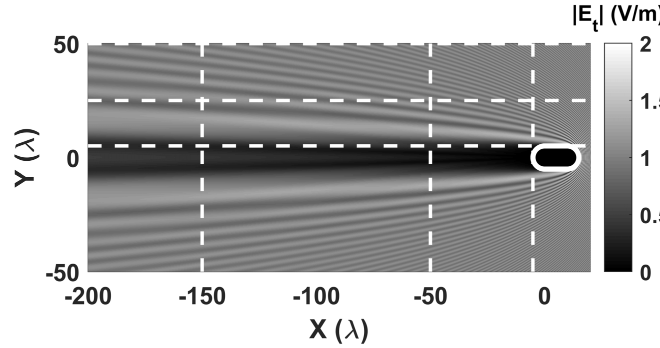

Fig. 16. Magnitude of the total electric field computed with MoM (TM case). The scatterer is illustrated in Fig. 10 and represented by a white solid contour. The dashed lines show the positions of the cuts in which fields are displayed in Fig. 17.

D. Computational complexity

The computation time required for the proposed approach is compared with the time required by an MoM-FMM solver. The reference test consists in computing the currents on an infinite cylinder with a circular cross section with a TM plane-wave excitation (see Section IV-A1), for an increasing radius. The MoM solution is obtained by solving the electric field integral equation (EFIE), using the pulse basis and testing functions, and is accelerated with the FMM for a fair comparison with the method presented in this article. The solution is computed iteratively using the generalized minimal residual error (GMRES) [44], for which the classical PO solution is used as the initial guess. The iterative process is stopped when the norm of the residual is smaller than 10^{-5}. The number of iterations is reduced by means of a sparse approximate

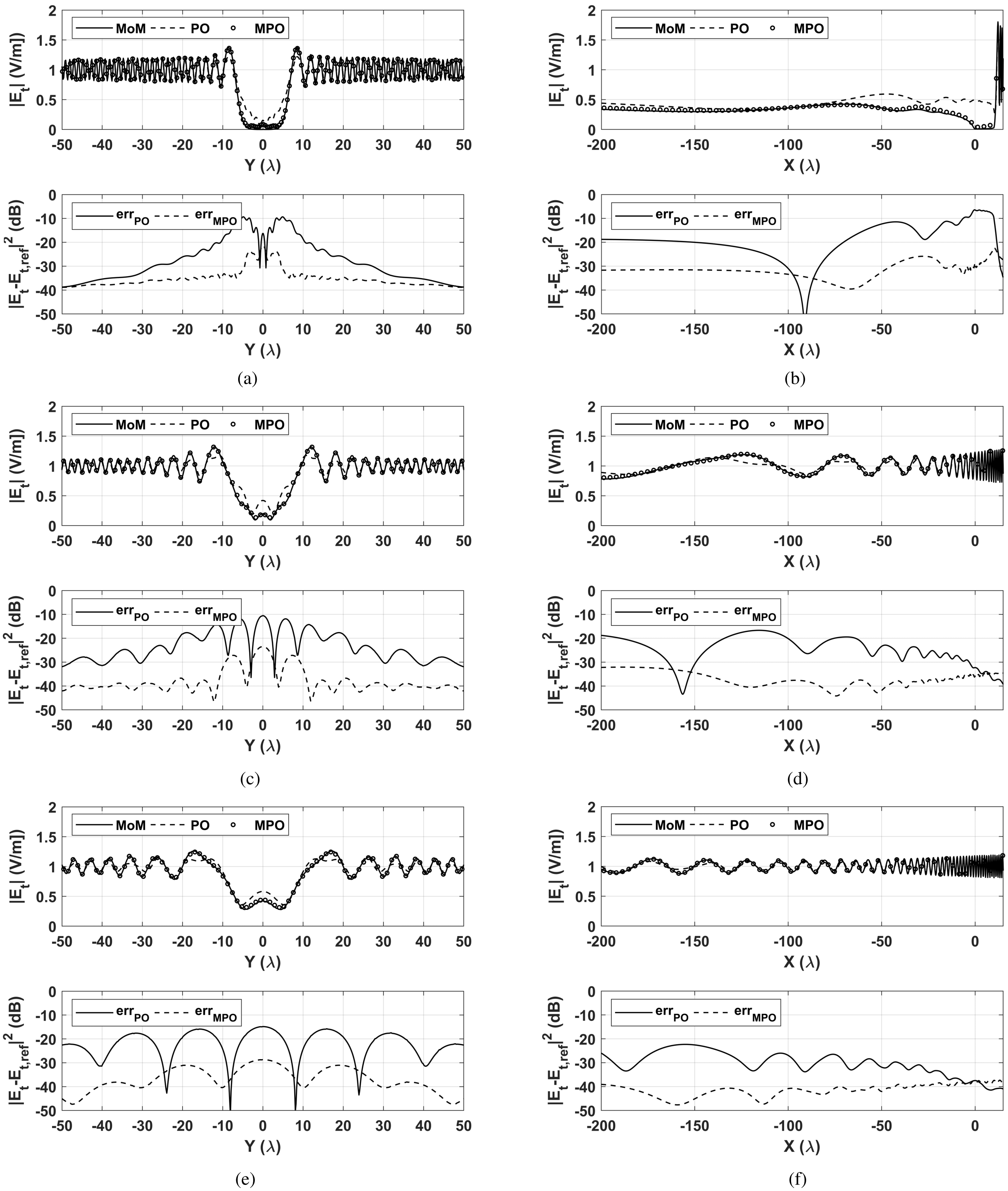

Fig. 17. Comparison of the total electric field of the problem described in Fig. 10 computed by MoM, the classical PO, and the method proposed in this article (MPO) for a TM incidence. The absolute error in a logarithmic scale is also provided for the six cuts drawn in Fig. 16. (a) $X = -5.1\lambda$. (b) $Y = 5.1\lambda$. (c) $X = -50\lambda$. (d) $Y = 25\lambda$. (e) $X = -150\lambda$. (f) $Y = 50\lambda$.

inverse (SAI) preconditioner [45], with a nonzero pattern identical to the near-field impedance matrix. The MPO solution is taken after three iterations [i.e., MPO(2)], as presented in the aforementioned examples. For both methods, the size of the FMM groups is chosen optimally with respect to the FMM preparation time. This comprises the time T_{pat} required for the computation of the radiation patterns of the transmitting and receiving groups [see (14) and (15)], the time T_{near} for the brute-force computation of the near-field interactions, and the time T_{trans} for the translation operator [see (29)]. Those

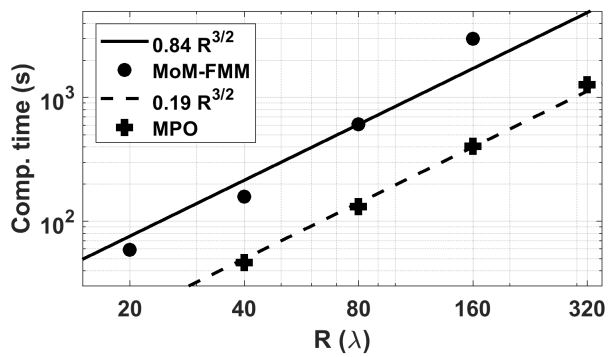

Fig. 18. Total CPU time for both MoM-FMM and MPO for different radii of an infinite cylinder with a circular section under TM plane-wave incidence.

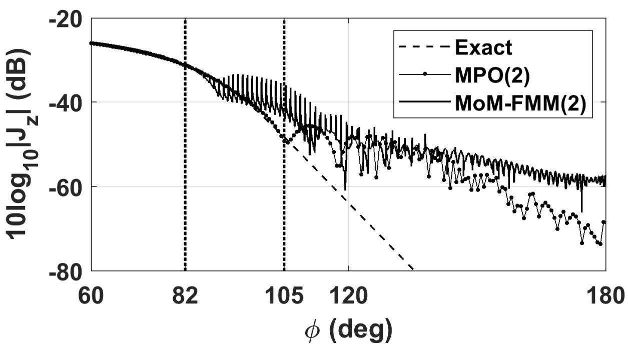

Fig. 19. Current distribution for a cylinder with a circular cross section and a radius $R = 100\lambda$. The vertical dotted lines correspond to 82° and 105°.

are computed and stored prior to the iteration process, and thus do not depend on the number of iterations. Considering a problem with N unknowns divided among G groups and H unknowns per group, so that $GH = N$, the abovementioned times are expressed as

$$T_{\text{pat}} = C_1 N H \tag{19}$$

$$T_{\text{near}} = C_2 N H \tag{20}$$

$$T_{\text{trans}} = C_3 G^2 H = C_3 \frac{N^2}{H} \tag{21}$$

where C_1, C_2, and C_3 are platform- and software-dependent. The value of H that minimizes the total construction time $T_{\text{constr}} = T_{\text{pat}} + T_{\text{near}} + T_{\text{trans}}$ is

$$H = \sqrt{\frac{C_3}{C_1 + C_2} N}$$

which leads to a computational complexity of $\mathcal{O}(N^{3/2})$. For the considered problems and the platform used, the constants C_1, C_2, and C_3 are of the order 10^{-5}, 10^{-3}, and 10^{-4}, respectively. Once those constants are known, the total CPU time for the modified PO is estimated using (19)–(21), where the time for the three iterations is neglected, as it is marginal compared with the FMM preparation (see Table I). This is not the case for the MoM-FMM, for which the number of iterations is not known *a priori* and the time required for reaching convergence is not negligible compared with the total computation time.

For each considered radius, the maximal mesh element size is $\lambda/15$ for the MoM-FMM and $\lambda/8$ for the proposed approach. To provide a fair comparison, the computation time is expressed with respect to the electrical size of the scatterer rather than the number of unknowns. The computations are performed on Intel i7-4790 at 3.6 GHz CPU workstation with 32 GB RAM. The computation time versus the cylinder radius is shown in Fig. 18. One can observe that the theoretical complexity order is met and is the same for both methods, whereas the MPO has a smaller absolute computation time than the MoM-FMM (factor 3.4–7.4 depending on the considered radii). The total CPU time T_{tot} includes the computation of the FMM precomputations (i.e., the radiation patterns of the transmitting/receiving groups and the translation operator), as well as the computation of the near interaction impedance matrices for both methods. In addition, the MoM-FMM solution also requires the building of the preconditioner and converges after an *a priori* unknown number of iterations, usually growing with the electrical size of the object [46]. The proposed modification of the PO is attractive in this respect, since the number of iterations is fixed and limited to a maximum of three, after which no significant improvement on the accuracy is expected. Those three iterations have a marginal cost (T_{iter}, with $T_{\text{sol}} = T_{\text{iter}} \cdot N_{\text{iter}}$) in terms of computation time, negligible compared with the FMM preparation and the near interaction computations. We emphasize that, even when using the classical PO solution as the initial guess, the MoM-FMM solution obtained after three iterations is less accurate than the converged MPO(2). This is observed in Fig. 19, where the MoM-FMM solution after three iterations starts to deviate from the exact solution at 82°, whereas the MPO(2) curve is in very good agreement with the reference currents up to 105°. In this region, the nonconverged MoM-FMM currents are oscillating due to the division of the scatterer in the FMM subdomains, and those currents are significantly less accurate than the MPO(2).

TABLE I

COMPARISON OF THE COMPUTATION TIME FOR THE MOM AND THE MPO, FOR AN INFINITE CYLINDER WITH CIRCULAR CROSS SECTION AND A RADIUS OF $R = 160\lambda$

	MoM-FMM	(N_{iter})	MPO	(N_{iter})
T_{pat}	2 s		4 s	
T_{trans}	284 s		217 s	
T_{near}	562 s		185 s	
T_{precond}	40 s		N.A.	
T_{iter}	1.02 s	(2044)	2 s	(3)
T_{sol}	2086 s		6 s	
T_{tot}	2934 s		412 s	

Table I summarizes the detailed CPU time for both methods for a cylinder of radius $R = 160\lambda$. It is observed that the time for one MPO iteration (T_{iter}) is roughly two times larger than that for an MoM-FMM iteration; that is because the sources of magnetic field are both electric and magnetic in the case of MPO, whereas it is purely electric for the MoM-FMM (assuming a PEC reflector).

V. CONCLUSION AND PERSPECTIVES

A modified version of the classical PO solution has been proposed in this work. This method provides a more accurate solution where the classical PO fails, namely, in the forward region, by finding an approximation of the currents induced on the shadowed part of the object, where the classical PO assumes zero currents. Those currents are obtained by illuminating the shadowed part of the scatterer with equivalent currents flowing on a surface surrounding the object, acting as the source of the new incident fields.

The simulation results show that the new approach significantly enhances the accuracy of the estimated scattered fields compared with the classical PO, in particular for the observation points located behind the scatterer. Indeed, the results displayed in Fig. 17 show that the absolute error in this region is below −30 dB, which is reduced by 10–15 dB with respect to the classical PO. In particular, the method is useful for the nose-on illumination problems or when the surface exhibits discontinuities (Section IV-B), as well as for a TE-polarized incident field, where the classical PO delivers a poor approximation in the nonspecular region (Section IV-A2).

The computation of those equivalent currents is the bottleneck of the algorithm and is, thus, accelerated in two ways. On the one hand, for the interactions between the basis and testing groups on S and S' that are far from each other, a lower complexity is reached with the help of the FMM, which reduces the complexity from $\mathcal{O}(N^2)$ to $\mathcal{O}(N^{3/2})$, with N being the number of basis and testing functions. For close groups, on the other hand, the integration has to be computed explicitly with (5) and (6). These integrals require a large number of integration points due to the singularity of Green's function for small argument. This constraint is alleviated by performing an analytical singularity extraction without the loss of accuracy (Appendix D). The simulation results have shown that, although the asymptotic complexity of this method is the same as that for the MoM, smaller absolute CPU times (factor of order 1/5) are achieved with the proposed method for scatterers having the same electrical size.

The proposed PO modification has been presented for the convex and slightly concave isolated objects, although many practical problems involve internal reflections (e.g., convex scatterers) or interactions between many scatterers. Such problems are generally analyzed using IPO [10], [11], [14], where the method proposed here could provide a better starting point for the iterative process.

Appendix A
Explicit Derivation of the Radiated Fields

Let assume a 2-D TM problem, where the electric field of the wave illuminating the object is parallel to the axis of the PEC cylinder, as depicted in Fig. 1. Under these conditions, the initial PO currents on the object are given by

$$\mathbf{J}_{\mathrm{PO}} = [0, 0, \mathrm{J}^z_{\mathrm{PO}}]^{\mathrm{T}}, \quad \mathbf{M}_{\mathrm{PO}} = \mathbf{0}. \tag{22}$$

The currents $\mathbf{J}_{\mathrm{e}}$ and $\mathbf{M}_{\mathrm{e}}$ are obtained with the help of (3) and (4), where $\mathbf{E}_{\mathrm{t}} = \mathbf{E}_{\mathrm{i}} + \mathbf{E}_{\mathrm{PO}}$ and $\mathbf{H}_{\mathrm{t}} = \mathbf{H}_{\mathrm{i}} + \mathbf{H}_{\mathrm{PO}}$. The fields $\mathbf{E}_{\mathrm{PO}}$ and $\mathbf{H}_{\mathrm{PO}}$ radiated by the PO initial currents are computed as

$$\mathrm{E}^z_{\mathrm{PO}} = -j\omega\mu \int_S \mathrm{J}^z_{\mathrm{PO}}\, g \, \mathrm{d}S \tag{23}$$

$$\mathrm{H}^x_{\mathrm{PO}} = \int_S \mathrm{J}^z_{\mathrm{PO}} \frac{\partial g}{\partial y} \, \mathrm{d}S \tag{24}$$

$$\mathrm{H}^y_{\mathrm{PO}} = -\int_S \mathrm{J}^z_{\mathrm{PO}} \frac{\partial g}{\partial x} \, \mathrm{d}S. \tag{25}$$

The equivalent currents on S' are expressed as

$$\mathbf{J}_{\mathrm{e}} = [0, 0, \mathrm{J}^z_{\mathrm{e}}]^{\mathrm{T}}, \quad \mathbf{M}_{\mathrm{e}} = [\mathrm{M}^x_{\mathrm{e}}, \mathrm{M}^y_{\mathrm{e}}, 0]^{\mathrm{T}}. \tag{26}$$

The updated electrical current is obtained with the help of (12), where the magnetic field $\mathbf{H}_{\mathrm{e}}$ radiated by $\mathbf{J}_{\mathrm{e}}$ and $\mathbf{M}_{\mathrm{e}}$ is expressed as

$$\begin{aligned}\mathrm{H}^x_{\mathrm{e}} = &-\int_{S'} j\omega\epsilon \left[\mathrm{M}^x_{\mathrm{e}}\, g + \frac{1}{k^2}\left(\mathrm{M}^x_{\mathrm{e}} \frac{\partial^2 g}{\partial x^2} + \mathrm{M}^y_{\mathrm{e}} \frac{\partial^2 g}{\partial x \partial y}\right)\right] \mathrm{d}S' \\ &+ \int_{S'} \mathrm{J}^z_{\mathrm{e}} \frac{\partial g}{\partial y} \, \mathrm{d}S'\end{aligned} \tag{27}$$

$$\begin{aligned}\mathrm{H}^y_{\mathrm{e}} = &-\int_{S'} j\omega\epsilon \left[\mathrm{M}^y_{\mathrm{e}}\, g + \frac{1}{k^2}\left(\mathrm{M}^x_{\mathrm{e}} \frac{\partial^2 g}{\partial x \partial y} + \mathrm{M}^y_{\mathrm{e}} \frac{\partial^2 g}{\partial y^2}\right)\right] \mathrm{d}S' \\ &- \int_{S'} \mathrm{J}^z_{\mathrm{e}} \frac{\partial g}{\partial x} \, \mathrm{d}S'.\end{aligned} \tag{28}$$

The partial derivatives involved in the above equations are provided in Appendix D. This example can be derived similarly for the TE problem.

Appendix B
Translation Operator

The translation operator used here for the FMM interactions is defined as [33], [47]

$$T(\mathbf{r}_{n'm'}, \alpha) = \sum_{p=-P}^{P} H_p^{(2)}(k|\mathbf{r}_{n'm'}|) e^{-jp\left(\phi_{n'm'} - \alpha + \frac{\pi}{2}\right)} \tag{29}$$

where $|\mathbf{r}_{n'm'}|$ is the distance between the centers of the source and testing groups, α is the angle defining the unit circle, and $\phi_{n'm'}$ is the angle of $\mathbf{r}_{n'm'}$ along $\hat{\mathbf{x}}$. The error by multipole decomposition can be reduced by performing the above summation over larger values of P. Nevertheless, the series diverges when P is larger than the argument of Hankel's function. The divergence is avoided by increasing the minimal distance between the groups, at the price of a higher computational complexity. More information regarding the selection of P is found in [47]. Note that the FMM is only valid for the groups that are sufficiently far from each other. If the groups are too close (as a rule of thumb, the distance between the centers is less than two times the size of the group bounding box), the multipole expansion does not hold anymore. This phenomenon is reported as the "violation of the addition theorem" in [33]. The function $T(r_{mn}, \alpha)$ is a band-limited function with respect to α, such that it requires a number of integration points $Q \sim \mathcal{O}(P)$ [33].

Appendix C
FMM for the Derivatives of Green's Function

Equation (13) corresponds to the multipole decomposition of 2-D Green's function, which consists of a product of the radiation pattern of the source group, a translation function, and the radiation pattern of the receiving group.

The multipole decomposition also holds for the derivatives of Green's function, and is listed as follows. Since the differential operators in(5) and (6) apply on the observation coordinates, the differentiation operates solely on the receiving pattern of (15)

$$P(x, y, \hat{\alpha}) = \exp(-jk\hat{\alpha}\cdot\mathbf{r}_{mm'}) \tag{30}$$

$$\frac{\partial}{\partial x}P(\cdot) = P(\cdot)jk\cos\alpha \tag{31}$$

$$\frac{\partial}{\partial y}P(\cdot) = P(\cdot)jk\sin\alpha \tag{32}$$

$$\frac{\partial^2}{\partial x^2}P(\cdot) = -P(\cdot)k^2\cos^2\alpha \tag{33}$$

$$\frac{\partial^2}{\partial y^2}P(\cdot) = -P(\cdot)k^2\sin^2\alpha \tag{34}$$

$$\frac{\partial^2}{\partial xy}P(\cdot) = -P(\cdot)k^2\cos\alpha\sin\alpha. \tag{35}$$

Appendix D
Analytical Singularity Extraction

We provide here the expression of Green's function and its partial derivatives as well as their singular part around the origin. Thanks to the analytical singularity integration [see (16)], the number of sampling points is significantly reduced when the argument of Green's function gets small. In the following equations, $\rho = |\mathbf{r}' - \mathbf{r}|$, with $\mathbf{r} = x\,\hat{\mathbf{x}} + y\,\hat{\mathbf{y}}$ and $\mathbf{r}' = x'\,\hat{\mathbf{x}} + y'\,\hat{\mathbf{y}}$:

$$G(x) = \frac{-j}{4}H_0^{(2)}(k\rho) \tag{36}$$

$$g_s(x) = \frac{-j}{2\pi}\log(k\rho/2) \tag{37}$$

$$\frac{\partial}{\partial x}G = \frac{-jk}{4}H_1^{(2)}(k\rho)\frac{x'-x}{\rho} \tag{38}$$

$$\frac{\partial}{\partial x}G_s = \frac{1}{2\pi}\frac{x'-x}{\rho^2} \tag{39}$$

$$\frac{\partial}{\partial y}G = \frac{-jk}{4}H_1^{(2)}(k\rho)\frac{y'-y}{\rho} \tag{40}$$

$$\frac{\partial}{\partial y}G_s = \frac{1}{2\pi}\frac{y'-y}{\rho^2} \tag{41}$$

$$\frac{\partial^2}{\partial x^2}G = \frac{jk^2}{4\rho^2}\left(\frac{(x-x')^2}{2}\left(H_0^{(2)}(k\rho) - H_2^{(2)}(k\rho)\right) + \frac{(y-y')^2}{\rho}H_1^2(k\rho)\right) \tag{42}$$

$$\frac{\partial^2}{\partial x^2}G_s = \frac{-k^2}{8\pi}\left(1 + \frac{4}{k^2\rho^2} + 2\log(k\rho)\right) \tag{43}$$

$$\frac{\partial^2}{\partial y^2}G = \frac{jk^2}{4\rho^2}\left(\frac{(y-y')^2}{2}\left(H_0^{(2)}(k\rho) - H_2^{(2)}(k\rho)\right) + \frac{(x-x')^2}{\rho}H_1^2(k\rho)\right) \tag{44}$$

$$\frac{\partial^2}{\partial y^2}G_s = \frac{\partial^2}{\partial x^2}g_s \tag{45}$$

$$\frac{\partial^2}{\partial x\partial y}G = \frac{jk}{4\rho^2}\left(\frac{k(x-x')(y-y')}{2}\left(H_0^{(2)}(k\rho) - H_2^{(2)}(k\rho)\right) + \frac{(x-x')(y-y')}{\rho}H_1^2(k\rho)\right) \tag{46}$$

$$\frac{\partial^2}{\partial x\partial y}G_s = \frac{4+k^2\rho^2}{4\pi\rho^4}(x-x')(y-y'). \tag{47}$$

All results involving G_s can be integrated analytically.

References

[1] B. Le Lepvrier, R. Loison, R. Gillard, P. Pouliguen, P. Potier, and L. Patier, "A new hybrid method for the analysis of surrounded antennas mounted on large platforms," *IEEE Trans. Antennas Propag.*, vol. 62, no. 5, pp. 2388–2397, May 2014.

[2] G. R. MacCartney, S. Deng, S. Sun, and T. S. Rappaport, "Millimeter-wave human blockage at 73 GHz with a simple double knife-edge diffraction model and extension for directional antennas," in *Proc. IEEE 84th Veh. Technol. Conf. (VTC-Fall)*, Sep. 2016, pp. 1–6.

[3] M. Falconi, D. Comite, A. Galli, D. Pastina, P. Lombardo, and F. Marzano, "Forward scatter radar for air surveillance: Characterizing the target-receiver transition from far-field to near-field regions," *Remote Sens.*, vol. 9, no. 1, p. 50, Jan. 2017. [Online]. Available: https://www.mdpi.com/2072-4292/9/1/50

[4] J. Glaser, "Bistatic RCS of complex objects near forward scatter," *IEEE Trans. Aerosp. Electron. Syst.*, vol. AES-21, no. 1, pp. 70–78, Jan. 1985.

[5] J. Perez and M. F. Catedra, "Application of physical optics to the RCS computation of bodies modeled with NURBS surfaces," *IEEE Trans. Antennas Propag.*, vol. 42, no. 10, pp. 1404–1411, Oct. 1994.

[6] M. Potgieter, "Bistatic RCS calculations of complex realistic targets using asymptotic methods," in *Proc. Int. Workshop Comput., Electromagn., Mach. Intell. (CEMi)*, Nov. 2018, pp. 23–24.

[7] M. Shafieipour, J. Aronsson, and V. Okhmatovski, "On error controlled computing of the near electromagnetic fields in the shade regions of electrically large 3D objects," in *Proc. URSI Int. Symp. Electromagn. Theory (EMTS)*, Aug. 2016, pp. 203–206.

[8] R. Ross, "Radar cross section of rectangular flat plates as a function of aspect angle," *IEEE Trans. Antennas Propag.*, vol. AP-14, no. 3, pp. 329–335, May 1966.

[9] F. Obelleiro-Basteiro, J. Luis Rodriguez, and R. J. Burkholder, "An iterative physical optics approach for analyzing the electromagnetic scattering by large open-ended cavities," *IEEE Trans. Antennas Propag.*, vol. 43, no. 4, pp. 356–361, Apr. 1995.

[10] R. J. Burkholder, C. Tokgoz, C. J. Reddy, and P. H. Pathak, "Iterative physical optics: Its not just for cavities anymore [EM wave propagation]," in *Proc. IEEE Antennas Propag. Soc. Int. Symp.*, vol. 1A, Jul. 2005, pp. 18–21.

[11] A. Thomet, G. Kubicke, C. Bourlier, and P. Pouliguen, "Improvement of iterative physical optics using the physical optics shadow radiation," *Prog. Electromagn. Res. M*, vol. 38, pp. 1–13, 2014.

[12] A. Gorji, B. Zakeri, and R. C. Janalizadeh, "Physical optics analysis for RCS computation of a relatively small complex structure," *Appl. Comput. Electromagn. Soc. J.*, vol. 29, pp. 530–540, Jul. 2014.

[13] R. J. Burkholder, C. Tokgoz, C. J. Reddy, and W. O. Coburn, "Iterative physical optics for radar scattering predictions," *J.-Appl. Comput. Electromagn. Soc.*, vol. 24, no. 2, pp. 241–258, Apr. 2009.

[14] I. Gershenzon, Y. Brick, and A. Boag, "Shadow radiation iterative physical optics method for high-frequency scattering," *IEEE Trans. Antennas Propag.*, vol. 66, no. 2, pp. 871–883, Feb. 2018.

[15] M. F. Catedra, C. Delgado, and I. G. Diego, "New physical optics approach for an efficient treatment of multiple bounces in curved bodies defined by an impedance boundary condition," *IEEE Trans. Antennas Propag.*, vol. 56, no. 3, pp. 728–736, Mar. 2008.

[16] R. F. Harrington, *Time-Harmonic Electromagnetic Fields*. New York, NY, USA: McGraw-Hill, 1961.

[17] A. Boag and C. Letrou, "Multilevel fast physical optics algorithm for radiation from non-planar apertures," *IEEE Trans. Antennas Propag.*, vol. 53, no. 6, pp. 2064–2072, Jun. 2005.

[18] P. Pathak, W. Burnside, and R. Marhefka, "A uniform GTD analysis of the diffraction of electromagnetic waves by a smooth convex surface," *IEEE Trans. Antennas Propag.*, vol. AP-28, no. 5, pp. 631–642, Sep. 1980.

[19] M. Balasubramanian, "UTD diffraction by smooth convex NURBS surfaces and its application to efficient hybrid UTD/FEBI-MLFMM methods," Ph.D. dissertation, Dept. ingegneria dell'informazione e scienze matematiche, Univ. Siena, Siena, Italy, Apr. 2015.

[20] S. Katz, A. Tal, and R. Basri, "Direct visibility of point sets," *ACM Trans. Graph.*, vol. 26, no. 3, pp. 1–11, Jul. 2007, doi: 10.1145/1276377.1276407.

[21] D. P. Xiang and M. M. Botha, "MLFMM-based, fast multiple-reflection physical optics for large-scale electromagnetic scattering analysis," *J. Comput. Phys.*, vol. 368, pp. 69–91, Sep. 2018. [Online]. Available: http://www.sciencedirect.com/science/article/pii/S0021999118302870

[22] G. Kubické, C. Bourlier, M. Delahaye, C. Corbel, N. Pinel, and P. Pouliguen, "Bridging the gap between the babinet principle and the physical optics approximation: Vectorial problem," *Radio Sci.*, vol. 48, no. 5, pp. 573–581, Sep. 2013.

[23] Y. M. Wu and W. C. Chew, "The modern high frequency methods for solving electromagnetic scattering problems (Invited Paper)," *Prog. Electromagn. Res.*, vol. 156, pp. 63–82, 2016.

[24] V. A. Fock, *Electromagnetic Diffraction and Propagation Problems*. New York, NY, USA: Pergamon, 1965, ch. 2, pp. 10–22.

[25] S.-E. Sandström, "An extension of the fock current distribution functions," *AEU Int. J. Electron. Commun.*, vol. 66, no. 7, pp. 540–546, Jul. 2012. [Online]. Available: http://www.sciencedirect.com/science/article/pii/S1434841111002895

[26] Y. Z. Umul, "Modified theory of physical optics," *Opt. Express*, vol. 12, no. 20, pp. 4959–4972, Oct. 2004. [Online]. Available: http://www.opticsexpress.org/abstract.cfm?URI=oe-12-20-4959

[27] W. C. Gibson, *The Method of Moments in Electromagnetics*, 2nd ed. Boca Raton, FL, USA: CRC Press, 2015.

[28] R. Coifman, V. Rokhlin, and S. Wandzura, "The fast multipole method for the wave equation: A pedestrian prescription," *IEEE Antennas Propag. Mag.*, vol. 35, no. 3, pp. 7–12, Jun. 1993.

[29] C.-C. Lu and W. C. Chew, "A multilevel algorithm for solving a boundary integral equation of wave scattering," *Microw. Opt. Technol. Lett.*, vol. 7, no. 10, pp. 466–470, Jul. 1994.

[30] J. Song, C.-C. Lu, and W. Cho Chew, "Multilevel fast multipole algorithm for electromagnetic scattering by large complex objects," *IEEE Trans. Antennas Propag.*, vol. 45, no. 10, pp. 1488–1493, Oct. 1997.

[31] I. van den Bosch, M. Acheroy, and J.-P. Marcel, "Design, implementation, and optimization of a highly efficient multilevel fast multipole algorithm," in *Proc. Comput. Electromagn. Workshop*, Aug. 2007, pp. 1–6.

[32] O. Ergul, "Fast and accurate analysis of homogenized metamaterials with the surface integral equations and the multilevel fast multipole algorithm," *IEEE Antennas Wireless Propag. Lett.*, vol. 10, pp. 1286–1289, Nov. 2011.

[33] W. C. Chew, E. Michielssen, J. M. Song, and J. M. Jin, Eds., *Fast and Efficient Algorithms in Computational Electromagnetics*. Norwood, MA, USA: Artech House, 2001.

[34] E. Darve, "The fast multipole method: Numerical implementation," *J. Comput. Phys.*, vol. 160, no. 1, pp. 195–240, May 2000. [Online]. Available: http://www.sciencedirect.com/science/article/pii/S0021999100964519

[35] D. R. Wilton, S. M. Rao, and A. W. Glisson, "Electromagnetic scattering by arbitrary surfaces," Rome Air Develop. Center, Griffiss AFG, Red Bank, NY, USA, Tech. Rep. RADC-TR-79-325, Mar. 1980.

[36] D. Wilton, S. Rao, A. Glisson, D. Schaubert, O. Al-Bundak, and C. Butler, "Potential integrals for uniform and linear source distributions on polygonal and polyhedral domains," *IEEE Trans. Antennas Propag.*, vol. AP-32, no. 3, pp. 276–281, Mar. 1984.

[37] T. W. Dawson, "On the singularity of the axially symmetric Helmholtz Green's function, with application to BEM," *Appl. Math. Model.*, vol. 19, no. 10, pp. 590–600, Oct. 1995. [Online]. Available: http://www.sciencedirect.com/science/article/pii/0307904X95000804

[38] D. Miron, "The singular integral problem in surfaces," *IEEE Trans. Antennas Propag.*, vol. 31, no. 3, pp. 507–509, May 1983.

[39] S.-W. Lee, J. Boersma, C.-L. Law, and G. Deschamps, "Singularity in Green's function and its numerical evaluation," *IEEE Trans. Antennas Propag.*, vol. AP-28, no. 3, pp. 311–317, May 1980.

[40] G. Kubicke and C. Bourlier, "A fast hybrid method for scattering from a large object with dihedral effects above a large rough surface," *IEEE Trans. Antennas Propag.*, vol. 59, no. 1, pp. 189–198, Jan. 2011, doi: 10.1109/tap.2010.2090470.

[41] F. Molinet, I. Andronov, and D. Bouche, *Asymptotic and Hybrid Methods in Electromagnetics*. London, U.K.: IET, 2008, ch. 3, p. 143.

[42] A. V. Osipov and S. A. Tretyakov, *Modern Electromagnetic Scattering Theory With Applications*. Chichester, U.K.: Wiley, 2017, ch. 8, p. 615.

[43] F. Weinmann, "Accurate prediction of EM scattering by wind turbines," in *Proc. 8th Eur. Conf. Antennas Propag. (EuCAP)*, The Hague, The Netherlands, Apr. 2014, pp. 2317–2321.

[44] Y. Saad and M. H. Schultz, "GMRES: A generalized minimal residual algorithm for solving nonsymmetric linear systems," *SIAM J. Sci. Stat. Comput.*, vol. 7, no. 3, pp. 856–869, Jul. 1986.

[45] P. L. Rui and R. S. Chen, "An efficient sparse approximate inverse preconditioning for FMM implementation," *Microw. Opt. Technol. Lett.*, vol. 49, no. 7, pp. 1746–1750, 2007.

[46] N. A. Gumerov and R. Duraiswami, "Fast solution of multiple scattering problems," in *Fast Multipole Methods for the Helmholtz Equation in Three Dimensions*. Amsterdam, The Netherlands: Elsevier, 2004, p. 471.

[47] S. Ohnuki and W. Cho Chew, "Numerical accuracy of multipole expansion for 2-D MLFMA," *IEEE Trans. Antennas Propag.*, vol. 51, no. 8, pp. 1883–1890, Aug. 2003.

Thomas Pairon was born in Namur, Belgium, in 1992. He received the B.Sc. and M.Sc. degrees in electrical engineering from the Université catholique de Louvain, Louvain-la-Neuve, Belgium, in 2013 and 2015, respectively, where he is currently pursuing the Ph.D. degree with the Antenna Group and the Cosy Group.

In 2016, he received the FRS FNRS-FRIA four-year grant for pursuing his studies. His current research interests include scattering by large curved structures, numerical simulations of large antenna arrays, and propagation in indoor environment.

Christophe Craeye (Senior Member, IEEE) was born in Ronse, Belgium, in 1971. He received the B.E. degree in electrical engineering, and the B.Phil. and Ph.D. degrees in applied sciences from the Université catholique de Louvain (UCL), Louvain-la-Neuve, Belgium, in 1994 and 1998, respectively.

From 1994 to 1999, he was a Teaching Assistant with UCL, where he was involved in the research on the radar signature of the sea surface perturbed by rain, in collaboration with NASA and ESA. From 1999 to 2001, he was a Post-Doctoral Researcher with the Eindhoven University of Technology, Eindhoven, The Netherlands, where he was involved in wideband phased arrays devoted to the square kilometer array radio telescope. In this framework, he was also with the University of Massachusetts, Amherst, MA, USA, in 1999 and the Netherlands Institute for Research in Astronomy, Dwingeloo, The Netherlands, in 2001. In 2002, he started an antenna research activity at UCL, where he is currently a Professor. He was with the Astrophysics and Detectors Group, University of Cambridge, Cambridge, U.K., in 2011. His current research is funded by Région Wallonne, European Commission, ESA, FNRS, and UCL. His current research interests include finite antenna arrays, wideband antennas, small antennas, metamaterials, and numerical methods for fields in periodic media, with applications to communication and sensing systems.

Dr. Craeye was a recipient of the 2005–2008 Georges Vanderlinden Prize from the Belgian Royal Academy of Sciences in 2009. He served as an Associate Editor for the IEEE Transactions on Antennas and Propagation and the IEEE Antennas and Wireless Propagation Letters from 2011 to 2017.

Claude Oestges (Fellow, IEEE) received the M.Sc. and Ph.D. degrees in electrical engineering from the Université catholique de Louvain (UCLouvain), Louvain-la-Neuve, Belgium, in 1996 and 2000, respectively.

In 2001, he joined the Smart Antennas Research Group (Information Systems Laboratory), Stanford University, Stanford, CA, USA, as a Post-Doctoral Scholar. From 2002 to 2005, he was a Post-Doctoral Fellow of the Belgian Fonds de la Recherche Scientifique (FRS-FNRS) with the Microwave Laboratory, UCLouvain. He is currently a Full Professor with the Electrical Engineering Department, Institute for Information and Communication Technologies, Electronics and Applied Mathematics, UCLouvain. He has authored or coauthored three books and more than 200 journal articles and conference communications.

Dr. Oestges is also the Chair of the COST Action CA15104 IRACON from 2016 to 2020. He was a recipient of the 1999–2000 IET Marconi Premium Award and the IEEE Vehicular Technology Society Neal Shepherd Award in 2004 and 2012, respectively.